# VPS13D interacts with VCP/p97 and negatively regulates endoplasmic reticulum–mitochondria interactions

Yuanjiao Du[a,†], Jingru Wang[a,†], Juan Xiong[b], Na Fang[a], and Wei-Ke Ji[a,c,*]
[a]Department of Biochemistry and Molecular Biology, School of Basic Medicine, [b]Department of Anesthesiology, Tongji Hospital, Tongji Medical College, and [c]Cell Architecture Research Institute, Huazhong University of Science and Technology, Wuhan, Hubei 430030, China

**ABSTRACT** Membrane contact sites (MCSs) between the endoplasmic reticulum (ER) and mitochondria are emerging as critical hubs for diverse cellular events, and alterations in the extent of these contacts are linked to neurodegenerative diseases. However, the mechanisms that control ER–mitochondria interactions are so far elusive. Here, we demonstrate a key role of vacuolar protein sorting–associated protein 13D (VPS13D) in the negative regulation of ER–mitochondria MCSs. VPS13D suppression results in extensive ER–mitochondria tethering, a phenotype that can be substantially rescued by suppression of the tethering proteins VAPB and PTPIP51. VPS13D interacts with valosin-containing protein (VCP/p97) to control the level of ER-resident VAPB at contacts. VPS13D is required for the stability of p97. Functionally, VPS13D suppression leads to severe defects in mitochondrial morphology, mitochondrial cellular distribution, and mitochondrial DNA synthesis. Together, our results suggest that VPS13D negatively regulates the ER–mitochondria MCSs, partially through its interactions with VCP/p97.

## INTRODUCTION

Membrane contact sites (MCSs) between the endoplasmic reticulum (ER) and mitochondria are emerging as essential hubs for diverse cellular events in eukaryotic cells, including lipid and calcium transfer (Vance, 1990; Szabadkai *et al.*, 2006; Csordas *et al.*, 2010), mitochondrial quality control (Hamasaki *et al.*, 2013; McLelland *et al.*, 2018), mitochondrial division (Friedman *et al.*, 2011; Ji *et al.*,

2017) and fusion (Abrisch *et al.*, 2020), and mitochondrial DNA (mtDNA) synthesis (Murley *et al.*, 2013; Lewis *et al.*, 2016). At MCSs, organelle membranes are closely apposed and tethered with a gap distance of 10–40 nm but do not fuse (Csordas *et al.*, 2006; Friedman *et al.*, 2011). Multiple molecular tethers at ER–mitochondria MCSs have been identified, such as the ER–mitochondria encounter complex in yeast (Kornmann *et al.*, 2009), Mitofusin 2 (MFN2; de Brito and Scorrano, 2008), VDAC-GRP75-DJ-1-IP3R (Szabadkai *et al.*, 2006; Liu *et al.*, 2019), Fis1-Bap31 (Iwasawa *et al.*, 2011), VAPB-PTPIP51 (De Vos *et al.*, 2012), PDZD8 (Hirabayashi *et al.*, 2017), Mitoguardin 2 (Freyre *et al.*, 2019; Xu *et al.*, 2020), and VPS13A (Kumar *et al.*, 2018) in mammals. Although it is known that these proteins play a role in ER–mitochondria MSCs, the molecular mechanisms by which ER–mitochondria MSCs are controlled are largely unknown.

Alterations in the extent of ER-mitochondrial interactions are closely associated with major types of neurodegenerative diseases, including Alzheimer's disease (AD; Zampese *et al.*, 2011), Parkinson's disease (PD; Guardia-Laguarta *et al.*, 2014), and Amyotrophic Lateral Sclerosis (ALS; De Vos *et al.*, 2012). Mutations in the principal genes associated with familial AD (Bekris *et al.*, 2010; Zhang *et al.*, 2011), including amyloid precursor protein (APP), Presenilin 1, and Presenilin 2, enhanced the physical connections between the ER and mitochondria, as well as lipid metabolism (Area-Gomez *et al.*, 2012; Filadi *et al.*, 2016). Mutations in vesicle-associated membrane

protein B (VAPB), an ALS-related protein, resulted in an autosomal-dominant form of ALS, increased its affinity to its binding partner, PTPIP51, and consequently enhanced the interactions between the ER and mitochondria, correlating with increased $Ca^{2+}$ transfer into the mitochondria (De Vos et al., 2012). Additionally, the ALS-related protein TDP-43 can impair VAPB–PTPIP51 binding via glycogen synthase kinase 3β, resulting in the impairment of $Ca^{2+}$ uptake into the mitochondria and subsequent ATP production(Stoica et al., 2014). α-Synuclein, a hallmark of PD, has been reported to localize to ER–mitochondrial MCSs (Guardia-Laguarta et al., 2014), and PD-related mutations of α-Synuclein can bind to VAPB and disrupt the ER–mitochondria connections (Paillusson et al., 2017; Cali et al., 2019). However, the molecular mechanisms that safeguard the ER-mitochondrial interactions and their roles in diseases are largely elusive.

Human VPS13D consists of 4388 amino acids with a molecular weight of 492 kDa. It has been shown to harbor a ubiquitin-associated (UBA) domain, which is required for mitochondrial clearance in Drosophila (Anding et al., 2018). Mutations in VPS13D were recently identified in human neurodegenerative diseases (a new type of autosomal recessive spastic ataxia), and mitochondria in these patients showed severe defects in both morphology and function (Gauthier et al., 2018; Seong et al., 2018). Recent studies showed that VPS13D was localized to various organelle MCSs under diverse metabolic conditions, including the ER–mitochondria/peroxisome MCSs under normal conditions and mitochondria–lipid droplet junctions under starvation (Baldwin et al., 2021; Guillen-Samander et al., 2021; Wang et al., 2021). Here, we demonstrate a critical role of VPS13D in the negative regulation of ER–mitochondria MCSs. We show that VPS13D suppression results in extensive ER–mitochondrial tethering, a phenotype that was substantially rescued by suppression of the tethering proteins VAPB and PTPIP51. Furthermore, VPS13D interacts with VCP/p97 ATPase to dissociate VAPB, and VPS13D is required for p97 stability. Functionally, VPS13D suppression resulted in severe defects in mitochondrial morphology, mitochondrial distribution, and mitochondrial DNA (mtDNA) synthesis. Our findings reveal an important role of VPS13D in the negative regulation of ER–mitochondria MCSs and provide new insight into the mechanisms of mitochondrial dysfunctions implicated in relevant diseases.

## RESULTS

### VPS13D suppression results in extensive endoplasmic reticulum–mitochondria tethering

Given the role of VPS13D in determining mitochondrial morphology and function in disease, we explored whether it could affect the interactions between the ER and mitochondria, using live-cell confocal microscopy. Remarkably, small interfering RNA (siRNA)–mediated VPS13D suppression resulted in extensive ER–mitochondria tethering in U2OS cells by live-cell confocal microscopy (Figure 1A). The efficiency of siRNA-mediated VPS13D suppression was confirmed by Western blots (Supplemental Figure S1A) and quantitative PCR (qPCR; Supplemental Figure S1B). Increased interactions between the ER and mitochondria could be observed in both perinuclear and peripheral regions of cells (Figure 1, A–C). Our definition of perinuclear regions is described in Supplemental Figure S1C.

In addition, the extensive ER–mitochondria tethering induced by VPS13D suppression was quantitatively confirmed in a doxycycline (Dox)-inducible splitGFP-based ER–mitochondria MCS reporter U2OS cell line, which was a modified version of that used in a previous study (Cieri et al., 2018). Because the reconstitution of GFP (green fluorescent protein) was irreversible, a low concentration

(0.1 µM) and a short incubation time (12 h) of DOX were applied to avoid artificial tethering between the ER and mitochondria. Under this condition, both the ER and mitochondria appeared to be morphologically normal, and the GFP signals were specifically localized to the ER–mitochondria intersections (Supplemental Figure S1D). More importantly, we found that VPS13D suppression substantially increased the fluorescence intensity of splitGFP at sites where mitochondria were tethered to the ER (Supplemental Figure S1E).

To gain structural details of hypertethered ER–mitochondria contacts, we examined 3D reconstructed projections of these contacts in a perinuclear region of VPS13D-suppressed U2OS cells. We observed that the mitochondria were almost completely circumscribed by multiple ER tubules (Figure 1D). In addition, we directly examined ER-mitochondrial MCSs in VPS13D-suppressed U2OS cells by transmission electron microscopy (TEM). The ER–mitochondria MCSs were defined as regions within ~30-nm gaps between the ER and the outer mitochondrial membranes (OMM) under TEM (Csordas et al., 2006). Compared with the controls, VPS13D suppression caused substantial increases in both the number and length of ER–mitochondria contacts (Figure 1, E and F).

In addition, we examined whether VPS13D regulated contacts between the ER and other organelles, including the Golgi apparatus, peroxisomes, early endosomes, and late endosomes/lysosomes. We did not detect any substantial morphological changes in these ER-associated MCSs upon VPS13D suppression in U2OS cells (Supplemental Figure S2).

Given that VPS13A, another member of the human VPS13 family, was reported to be a lipid transporter at ER–mitochondria MCSs (Kumar et al., 2018), we tested whether the suppression of VPS13A could alter the ER–mitochondria interactions. The siRNAs-mediated suppression of VPS13A failed to increase the ER–mitochondrial interaction substantially by live-cell confocal microscopy (Supplemental Figure S3, A and B). In contrast, VPS13A and VPS13D double suppression led to an increase in ER–mitochondria interactions to an extent similar to that of VPS13D suppression alone (Supplemental Figure S3, A and B). The efficiency of siRNA-mediated silencing of VPS13A was confirmed by qPCR (Supplemental Figure S3C). These results indicated that the extensive associations between the ER and mitochondria were specific to VPS13D suppression and suggested that VPS13A was not required in the ER–mitochondria hypertethering, as the hypertethering phenotype still existed in the VPS13A/D double-knockdown condition.

In addition, we examined the localization of endogenous VPS13D relative to ER–mitochondria MCSs by immunofluorescence (IF) using a polyclonal antibody against VPS13D, which was precleared as previously described (Valverde et al., 2019). IF experiments using this precleared antibody showed that VPS13D was preferentially present at the intersections between the ER and mitochondria (Supplemental Figure S3D, Top panel); however, IF signals of endogenous VPS13D almost completely disappeared upon VPS13D suppression (Supplemental Figure S3D, Bottom panel). We found that a substantial portion of endogenous VPS13D (49%) was present or enriched at the sites of mitochondria tethering to the ER (Supplemental Figure S3E); meanwhile, 79% of ER–mitochondria junctions were marked by endogenous VPS13D (Supplemental Figure S3F). As a negative control, we rotated the VPS13D image 90° relative to the ER image and quantified the percentage of VPS13D puncta or foci at the ER contacts. We found that the percentage of 90°-rotated VPS13D at ER contacts is substantially reduced (Supplemental Figure S3E), suggesting that the presence of VPS13D at ER contacts is significant and not due to chance. Our results are in accordance with a recent study (Guillen-Samander et al., 2021).
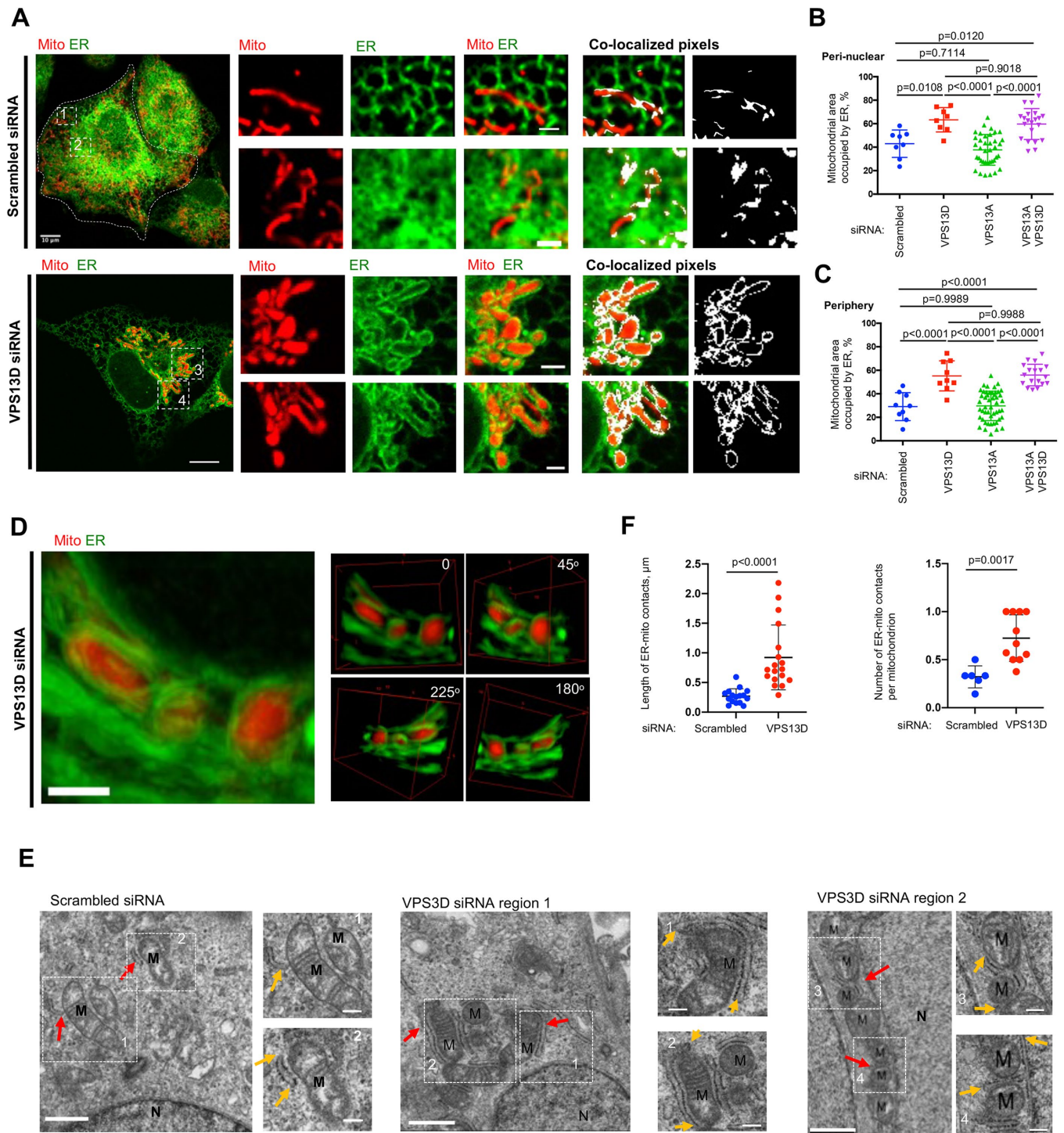
FIGURE 1: VPS13D suppression led to extensive ER–mitochondria tethering. (A) Confocal images of live U2OS cells labeled with mCherry-mito7 (red) and ER-mGFP (green) upon treatment with either scrambled siRNAs (top) or VPS13D-specific siRNAs (bottom). Left: whole cell image; Middle: ER–mitochondria intersections at cell periphery (top inset) or at perinuclear region (bottom inset); Eight: colocalization-based analysis of ER and mitochondria intersections, with white pixels showing potential contacts. (B, C) Quantification of extent of physical interactions between ER and mitochondria in perinuclear (B) and peripheral regions (C) based on colocalization-based analysis showing the percentage of mitochondrial surface covered by ER. For perinuclear region, scrambled ($n = 8$), VPS13D ($n = 8$), VPS13A ($n = 38$), or VPS13A&D siRNAs ($n = 21$) were analyzed. For peripheral region, scrambled ($n = 9$), VPS13D ($n = 9$), VPS13A ($n = 49$), or VPS13A&D siRNAs ($n = 18$) were analyzed. One-way ANOVA was followed by Tukey's multiple comparisons test. Mean ± SD. (D) Left: Maximum-intensity projection of 10 $z$ stacks (0.2 µm thickness in each stack) of confocal micrographs of ER–mitochondria MCSs at a perinuclear region. Right: 3D reconstruction of ER–mitochondria MCSs from four angles of view along the $z$-axis. (E) TEM micrographs showing examples of ER–mitochondria contacts in scrambled or VPS13D siRNAs–treated cells with two insets on right. Examples of ER–mitochondria contacts are indicated by red arrows, and

## VPS13D negatively regulates the level of VAPB

To understand how VPS13D negatively regulates ER–mitochondria interactions, we examined the cellular distribution of the known tethering proteins involved in ER–mitochondria MCSs by IF. Among these tethers, we found that the ER-resident tethering protein VAPB, known for tethering the ER to mitochondria with its binding partner PTPIP51, was strongly enriched at sites around mitochondria (Figure 2A, Middle panel), presumably at ER–mitochondria MCSs, upon VPS13D suppression. To test whether this enrichment is specific for VAPB, we examined the distribution of sec61, a general ER membrane marker, in cells depleted of VPS13D. The sec61 protein is almost evenly distributed all over the ER, though we can still see enhanced ER–mitochondria interactions in VPS13D-suppressed U2OS cells (Figure 2A, Bottom panel). This result suggests that the enrichment of VAPB at ER contacts is specific upon VPS13D suppression. The antibody against VAPB used in the IF assays was validated by siRNA-mediated suppression (Figure 2B).

To further confirm the enhanced enrichment of VAPB at ER–mitochondria MCSs in VPS13D-suppressed cells, we performed cell fractionation to examine the levels of VAPB and PTPIP51 in crude mitochondrial fractions, which contained pure mitochondria and mitochondria-associated membranes (MAMs). The level of VAPB increased strongly in the crude mitochondrial fractions in VPS13D-suppressed cells (Figure 2C). In addition, consistent with our imaging results, the cellular fractionation assays showed that levels of calnexin, a marker for MAMs, increased in crude mitochondrial fractions upon VPS13D suppression (Figure 2C), suggesting enhanced ER–mitochondria interactions. The suppression of VPS13D also increased the level of PTPIP51 in the crude mitochondrial fractions, but to a lesser extent than that of VAPB (Figure 2C). To test whether the increase of VAPB at MAMs/mitochondria only mirrors the increase of VAPB in whole-cell lysate, we examined the ratio of the VAPB level in scrambled cells to that in VPS13D-suppressed cells. We found that the level of VAPB increased upon VPS13D suppression in whole-cell lysate (WCL), but the extent of the increase in VAPB level in MAMs/mitochondrial fractions is significantly higher than that in WCL (Figure 2, C and D).

Previous work showed that overexpression of VAPB increased ER–mitochondria associations in NSC34 cells by EM (Radu Stoica et al., 2014). Consistently, we showed that overexpression of VAPB alone or coexpression of VAPB and PTPIP51 substantially enhanced the interactions between the ER and mitochondria in the ER–mitochondria MCSs reporter cell line by both confocal microscopy (Supplemental Figure S4, A–C) and flow cytometry (Supplemental Figure S4, D–H). These results indicated that the expression of VAPB alone or the coexpression of VAPB and PTPIP51 was able to promote ER–mitochondria interactions. Therefore, we hypothesized that VPS13D controlled the extent of ER–mitochondria MCSs by regulating the level of VAPB. To prove this, we tested whether suppression of both VAPB and its binding partner PTPIP51 could rescue the extensive tethering between the ER and mitochondria resulting from VPS13D suppression. Consistent with previous studies (De Vos et al., 2012), double suppression of VAPB and PTPIP51 robustly reduced ER–mitochondria interactions in wild type (WT) U2OS cells. The efficiency of siRNAs-mediated suppression of VAPB and PTPIP51 was confirmed by Western blots (Figure 2E). More importantly, we found that the suppression of VAPB and PTPIP51 substantially rescued the ER–mitochondria hypertethering at both perinuclear and peripheral regions in VPS13D-suppressed cells (Figure 2, F and G). This result suggested that VPS13D negatively regulates ER–mitochondria MCSs by modulating the levels of VPAB and PTPIP51.

## VPS13D interacts with p97 and is required for the stability of p97

Next, we investigated how VPS13D negatively regulates the level of VAPB at ER–mitochondrial MCSs. AAA-ATPase valosin-containing protein (VCP/p97) reportedly plays essential roles in ubiquitin-dependent protein degradation, dynamics, and homeostasis (Ye et al., 2001). p97 acts downstream of ubiquitin signaling events and utilizes the energy from ATP hydrolysis to extract its substrate proteins from membrane structures or multiprotein complexes (Ye et al., 2001). We found that endogenous VPS13D interacted with p97 by coimmunoprecipitation assays (Supplemental Figure S5A). Furthermore, we investigated which domains of VPS13D were responsible for interacting with p97 via GFP-trap assays. Our bioinformatics analysis predicted that VPS13D consists of an N-terminal lipid transfer domain, a UBA domain followed by a VPS13 adaptor-binding (VAB) domain, and a VPS13_C domain at its C-terminus (Figure 3A). The GFP-trap assays indicated that both the UBA domain and the VAB domain were capable of interacting with p97 (Figure 3B). In contrast, the C-terminal region of VPS13D (residues 3791–4363) failed to interact with p97, supporting the conclusion that VPS13D-p97 interaction is specific. p97 was predicted to harbor an N domain at the N-terminus and a D1/D2 domain at its C-terminus (Stolz et al., 2011; Supplemental Figure S5B, Top panel). Our GFP-trap assays showed that neither the N domain alone nor the D1/D2 domain alone was able to interact with VPS13D (Supplemental Figure S5B, Bottom panel), suggesting that both of these two domains of p97 were required for interaction with VPS13D.

The UBA domain of VPS13D was reported to bind to K63-, but not K48-linked ubiquitin chains, as determined by in vitro binding assays (Anding et al., 2018). We examined whether the VAB domain of VPS13D interacted with ubiquitin via IF. The IF results showed that VAB-GFP puncta were associated with both K63- and K48-linked ubiquitin chains in cells, with a preferential interaction with K63-linked ubiquitin (Supplemental Figure S5C). In addition, our GFP-trap assays confirmed the interactions between VAB-GFP and K63- and K48-linked ubiquitin chains (Supplemental Figure S5D). To further validate the VAB domain–ubiquitin interactions, GFP-trap assays using harsh wash buffers were performed to wash out proteins that were noncovalently bound to VAB-GFP. These results showed that neither K63- nor K48-linked ubiquitin was detectable (Supplemental Figure S5E), indicating that the VAB domain interacted with ubiquitin chains in a noncovalent manner and also that the VAB domain might not be conjugated by ubiquitin. In addition, our GFP-trap assays showed that p97 interacted with both K48- and K63-linked ubiquitin chains (Supplemental Figure S5F). Taken together, these lines of evidence

---

yellow arrows in insets indicate the extension of ER–mitochondria MCSs. M indicates mitochondria. MCSs under TEM were defined as regions within 30–nm gaps between ER and OMM (Csordas et al., 2006). (F) Quantification of length of ER–mitochondria MCSs (left panel) and number of ER–mitochondria MCSs per mitochondrion (right panel). In these quantifications, scrambled cells (n = 16 MCSs) and VPS13D siRNA–treated cells (n = 18 MCSs) are analyzed. Two-tailed unpaired Student's t test. Mean ± SD. Scale bar, 10 μm in whole-cell image and 2 μm in insets in A; 2 μm in D; 1 μm in big region and 0.2 μm in insets in E.
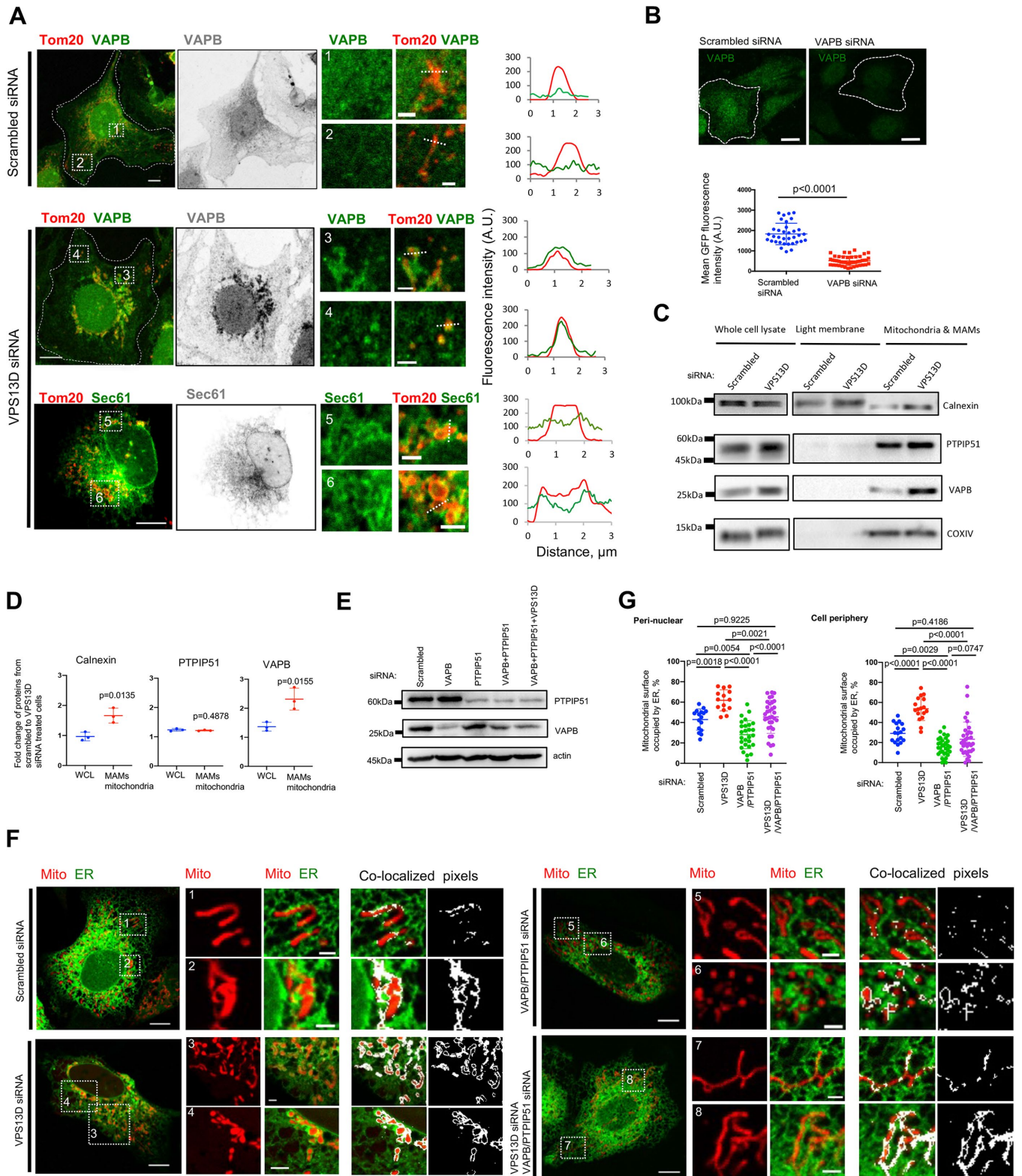
FIGURE 2: VPS13D negatively regulates the level of VAPB at ER contacts. (A) Immunostaining of U2OS cells treated with either scrambled (top) or VPS13D siRNAs (bottom) with anti-VAPB antibody (green, Top and Middle) or Sec61 (green, Bottom) and anti-Tom20 antibody (red). Left panel: merged image of whole cells; Middle panel: VAPB (gray, Top and Middle) or Sec61 (gray, Bottom); right panel showing two insets with one onset from cell perinuclear regions (top) and the other from cell periphery (bottom) with linescan analysis on the right. (B) Top: immunostaining of fixed U2OS cells treated with scrambled (left) or VAPB-specific siRNAs (right) with anti-VAPB antibody (green). Contrast range of images was set to 600–10,000 for both scrambled and VAPB siRNAs–treated cells. Bottom: the mean fluorescence of VAPB signals was quantified in scrambled ($n = 35$) and VAPB siRNA ($n = 46$)–treated cells. Mean intensity is defined as total fluorescence divided by the area of cells. Two-tailed unpaired Student's $t$ test. Mean ± SD. (C) Cell fractionations

indicated that the UBA domain and the VAB domain of VPS13D were independently associated with p97 and ubiquitin, suggesting that VPS13D, p97, and ubiquitin might form a ternary protein complex.

Previous studies demonstrated that p97 promoted the degradation of VAPB mutants (Papiani *et al.*, 2012; Baron *et al.*, 2014), but whether p97 could interact with and facilitate the degradation of WT-VAPB was unclear. Therefore, we examined the interactions between p97 and VAPB by GFP-trap assays, and we found that p97-GFP indeed interacted with endogenous VAPB (Supplemental Figure S5G). Because our results showed that VPS13D interacted with p97 and p97 also interacted with VAPB, we hypothesized that VPS13D might cooperate with the protein extractor p97 to dissociate the ER–resident tether VAPB from ER membranes, and consequently control the ER–mitochondria MCSs. To test this idea, we examined the effects of p97 on the degradation of WT-VAPB or two disease mutant variants of VAPB, VAPB-P56S and VAPB-T46I (Chen *et al.*, 2010), both of which were implicated in ALS. We found that overexpression of p97 substantially decreased the level of WT-VAPB, similarly to that of VAPB-P56S (Figure 3, C and D). One striking difference was that p97 overexpression failed to reduce the level of another VAPB mutant, VAPB-T46I (Figure 3, C and D), and this result was further confirmed in other cell lines, including HEK293, COS7, and HeLa cells (Supplemental Figure S5H), suggesting a new mechanism underlying the pathology of VAPB-T46I in ALS. To test whether VAPB-T46I is still sensitive to p97-mediated repression, but starts from a much higher level than the WT in the absence of p97 overexpression, we examined the level of VAPB and its pathogenic mutants in the absence of p97 overexpression in U2OS cells. We found that there is no substantial difference in the levels of VAPB-GFP, VAPB-GFP-T46I, and VAPB-GFP-P56S (Supplemental Figure S5I).

Next, we investigated whether VPS13D suppression affected p97. We initially examined the cellular distributions of endogenous p97 upon VPS13D suppression by IF using an anti-p97 antibody (Supplemental Figure S6A), which was validated by siRNA-mediated suppression (Supplemental Figure S6A, bottom panel). In control cells, p97 was mainly cytosolic, with a small fraction of p97 localizing to ER–mitochondria intersections in form of the punctae-like structures (Supplemental Figure S6A, top panel). We found a significant decrease in the fluorescence of endogenous p97 protein upon VPS13D suppression (Supplemental Figure S6A, middle panel), suggesting a correlation between VPS13D and p97 level. Therefore, we sought to explore whether VPS13D suppression affected the level of p97. Indeed, we found that the level of endogenous p97 was substantially reduced in response to VPS13D suppression (Figure 3, E and F). In addition, we explored whether VPS13D suppression affected the p97-VAPB interactions. Our GFP-trap assays showed that a significantly smaller amount of VAPB was coimmunoprecipatated

with p97-GFP in response to VPS13D suppression than in control cells (Figure 3G). We also noted that the level of p97-GFP was remarkably reduced in VPS13D-depleted cells (Figure 3, E and F), which may account for the smaller amount of VAPB coimmunoprecipitated by p97-GFP.

Given the correlation between VPS13D suppression and the reduced level of p97 in cells, we tested whether VPS13D was required for p97 protein stability by cycloheximide (CHX) chase assays. In control cells, endogenous p97 was stable, with a small but significant decrease over time, and p97 was readily detected after 30 h treatment of CHX (Figure 3, H and I). In contrast, the initial level of endogenous p97 was substantially lower, and p97 was almost undetectable after 17 h treatment of CHX in VPS13D-depleted cells (Figure 3, H and I), suggesting that p97 stability was compromised in response to VPS13D suppression.

To further confirm the role of p97 in the VPS13D-mediated regulation of ER–mitochondria interactions, we examined ER–mitochondria interactions in cells in which p97 was inhibited by its allosteric inhibitor NMS873, using live-cell confocal microscopy. We found that p97 inhibition resulted in extensive ER–mitochondria tethering in both perinuclear and periphery regions in a dosage-dependent manner (Figure 3, J and K), which mimicked the phenotype induced by the suppression of VPS13D.

In addition, we examined the ER–mitochondria interactions in p97 siRNA–treated U2OS cells. We found that siRNA-mediated p97 suppression significantly enhances the ER–-mitochondria interactions (Figure 3, L–O), consistent with the p97 inhibitor results (Figure 3, J and K). In addition, we examined the ER–mitochondria interactions in response to p97 overexpression in VPS13D-suppressed U2OS cells. Cells with VPS13D suppression and GFP vector expression substantially increase the ER–mitochondria connections (Figure 3N, Top panel; Figure 3O). Expression of p97-GFP moderately decreases, but does not completely rescue, the ER–mitochondria interaction in both perinuclear and peripheral regions in VPS13D-suppressed cells (Figure 3N, Bottom panel; Figure 3O), suggesting that, in addition to the level of p97, unknown pathways may also be responsible for the ER–mitochondria hypertethering phenotype observed in VPS13D-suppressed cells.

### VPS13D suppression perturbs mitochondrial morphology, mitochondrial distribution, and mtDNA synthesis

Next, we investigated whether the extensive ER–mitochondria tethering resulting from VPS13D suppression affected mitochondrial dynamics and functions. We tracked the dynamics of the ER–mitochondria interactions in either control or VPS13D-suppressed U2OS cells. Time-lapse image analysis demonstrated that mitochondrial motility was dramatically impaired in VPS13D-suppressed cells compared with that in controls (Figure 4A). Also, mitochondrial length

---

were analyzed by immunoblots for calnexin (ER and MAMs), PTPIP51 (a tether on the OMM), VAPB (a tether on the ER membrane), and COXIV (mitochondria). The WCLs were analyzed as a control. (D) Ratio of the levels of proteins (calnexin, PTPIP51, and VAPB) in scrambled cells to those in VPS13D-suppressed cells. Three independent assays were analyzed. Two-tailed unpaired Student's *t* test. Mean ± SD. (E) Immunoblots with antibodies against PTPIP51 and VAPB to demonstrate knockdown efficiency. (F) Confocal images of live U2OS cells expressing mCherry-mito7 and ER-mGFP upon treatment with scrambled, VPS13D siRNAs, VAPB+PTPIP51 siRNAs, or VPS13D+VAPB+PTPIP51 siRNAs. White pixels represented ER–mitochondria contacts. (G) Quantification of the extent of physical interactions between the ER and mitochondria at perinuclear (left panel) and peripheral regions (right panel) based on colocalization-based analysis showing the percentage of mitochondrial surface covered by ER. U2OS cells treated with scrambled (perinuclear: 16 ROIs; peripheral: 18 ROIs), VPS13D (perinuclear: 14 ROIs; peripheral: 17 ROIs), VAPB+PTPIP51 (perinuclear: 27 ROIs; peripheral: 33 ROIs), or VPS13D+VAPB+PTPIP51 (perinuclear: 33 ROIs; peripheral: 33 ROIs) siRNAs were analyzed. One-way ANOVA followed by Tukey's multiple comparisons test. Mean ± SD. Scale bar, 10 µm in whole cell image and 2 µm in insets in A, B, and F.
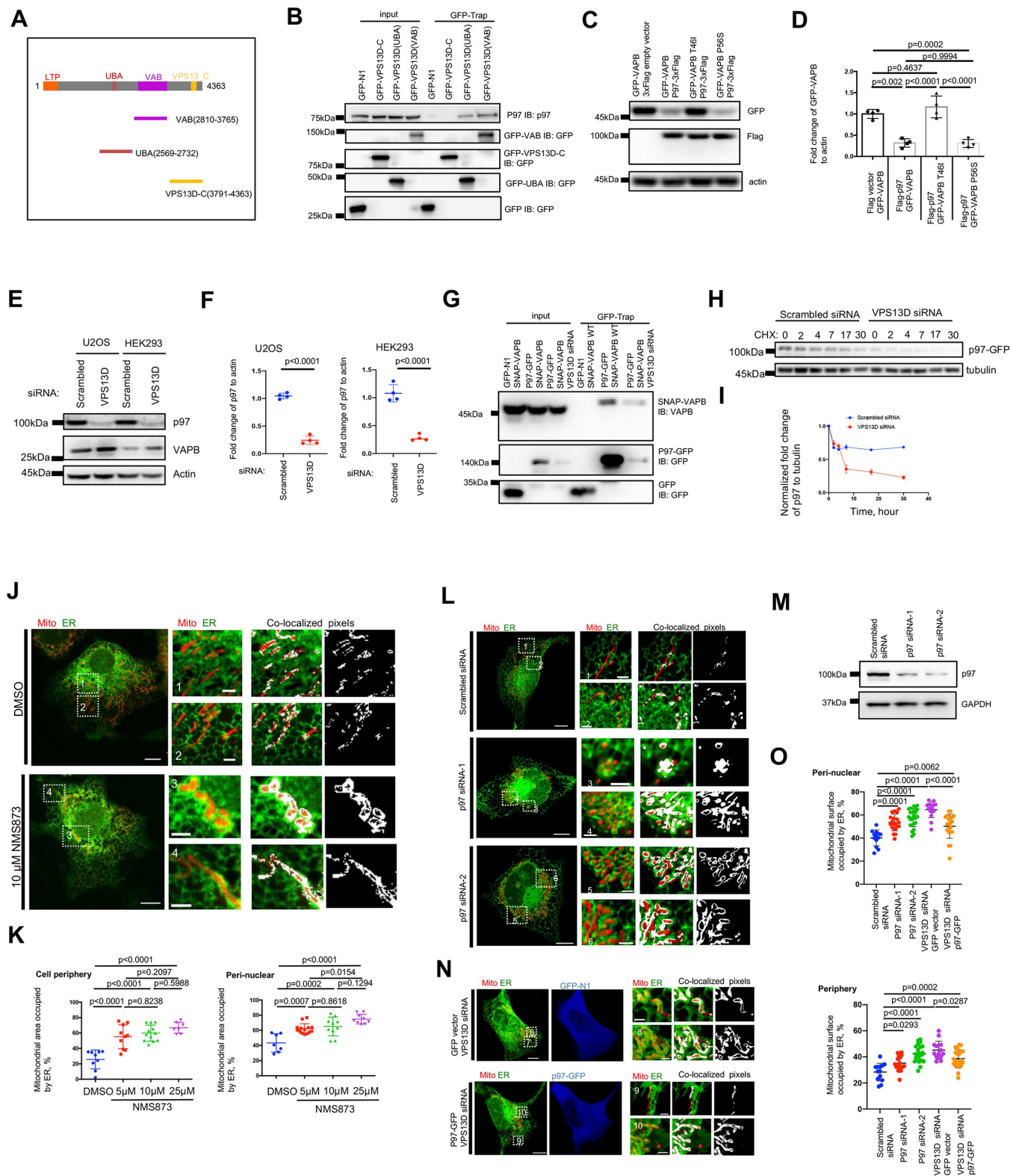
**FIGURE 3:** VPS13D interacts with p97, is required for p97 stability. (A) The domain organization of VPS13D and two truncation mutants. (B) GFP-trap assays indicated that the UBA and VAB domains independently interacted with p97. (C) Western blots showed the effects of p97 overexpression on GFP-VAPB (WT or disease mutant P56S and T46I). (D) Quantification of Western blots results . Three independent assays were performed. Ordinary one-way ANOVA, followed by Turkey's multiple comparisons test. Mean ± SD. (E) Western blots showed that VPS13D suppression decreased the level of endogenous p97 in U2OS and HEK293 cells. (F) Quantification of Western blots results in (E). Two-tailed unpaired Student's *t* test. Mean ± SD. (G) GFP-trap assays indicated that VPS13D suppression resulted in a reduced level of SNAP-VAPB coimmunoprecipitated with p97-GFP. (H) Western blots of cycloheximide chase assays showing the changes of the level of p97-GFP after CHX treatment. (I) Normalized ratio of p97-GFP to tubulin in

was significantly reduced (Figure 4B), in agreement with a previous study in *Drosophila* (Anding et al., 2018). In addition, we found that the majority of VPS13D-suppressed cells exhibited defects in mitochondrial distribution, in which mitochondria were clustered in perinuclear regions (Figure 4C), suggesting that VPS13D is required for mitochondrial transport.

We further explored whether these defects in mitochondrial morphology and distribution resulting from VPS13D suppression can be rescued by VAPB/PTPIP51 double knockdown or p97 overexpression. We found that both of these defects in mitochondrial perimeter and distribution are substantially rescued upon the simultaneous suppression of VAPB and PTPIP51 (Figure 4, B and C). Interestingly, p97 overexpression can significantly rescue, but not completely restore, these two defects (Figure 4, B and C), consistent with its effects on the ER-mitochondrial hypertethering phenotype.

Previous studies demonstrated that mtDNA synthesis was spatially and temporally regulated by ER–mitochondria MCSs (Murley et al., 2013; Lewis et al., 2016). Therefore, we sought to explore whether VPS13D regulated mtDNA synthesis. We performed siRNA-mediated suppression of VPS13D in a U2OS cell line stably expressing polG2-GFP, a marker of replicating mtDNA (Young et al., 2015). We found that replicating mtDNA localized to mitochondria at a density of 0.28 $\mu m^{-1}$ in control cells, with some polG2-GFP puncta preferentially localizing at the tips of mitochondria (Figure 4D, Top panel). In contrast, VPS13D suppression reduced the density of replicating mtDNA by a factor of 4 and strongly increased the size of replicating mtDNA, suggesting aggregation of mitochondrial nucleoids (Figure 4D, Bottom panel). In addition, the aggregated replicating mtDNA failed to localize to the tips of mitochondria in VPS13D-suppressed cells (Figure 4D, Bottom panel), suggesting defects in synthesis and distribution of replicating mtDNA. In addition, suppression of dynamin-related protein 1 (Drp1) or mitochondrial fission factor (Mff) significantly decreased the number of replicating mtDNA and caused the aggregation of replicating mtDNA (Figure 4E; Supplemental Figure S7, A–D), resembling the phenotype observed in VPS13D-suppressed cells. Suppression of MFN2 also significantly altered the density and size of replicating mtDNA, but to a lesser extent than that resulting from the suppression of Drp1 or Mff (Figure 4E; Supplemental Figure S6, E and F). Therefore, our results suggest that VPS13D suppression might lead to defects in mtDNA synthesis and distribution through affecting mitochondrial dynamics.

## DISCUSSION
Interfaces between the ER and mitochondria are critical for maintaining diverse cellular functions, and alterations in the extent of these contacts are linked to severe neurodegenerative diseases. However, the molecular mechanisms that negatively regulate the extent of ER–mitochondria MCSs are thus far largely elusive. Here, we demonstrated that VPS13D exerts quality control for ER–mitochondria interactions by negatively regulating the level of VAPB, partially through a p97-dependent pathway. Suppression of VPS13D caused intensive ER–mitochondria tethering. The UBA and VAB domains of VPS13D associated independently with p97 and ubiquitin. VPS13D was required for the stability of p97 protein. Functionally, VPS13D is required for mitochondrial morphology, mitochondrial cellular distribution, and mtDNA synthesis.

Our results show that the overexpression of p97-GFP moderately decreases, but does not completely rescue, the ER–mitochondria hypertethering in VPS13D-suppressed cells (Figure 3, N and O), suggesting that the p97-dependent pathway may not be solely responsible for this hypertethering phenotype. Therefore, multiple pathways may be responsible for the ER–mitochondria hypertethering in VPS13D suppressed cells. Because previous studies showed that VPS13 proteins, including VPS13D, bind and transfer glycerophospholipid and lipid fatty acid moieties in vitro, VPS13D is a potential lipid transfer protein (Kumar et al., 2018; Wang et al., 2021). One possibility is that the lipid transfer activities of VPS13D may be involved in the regulation of the ER–mitochondria interactions. The mechanisms of lipid transfer activities of VPS13D in the regulation of ER–mitochondria contacts warrant further investigations. In addition, a recent study (Guillen-Samander et al., 2021) shows that Rho GTPase Miro1 recruits VPS13D to mitochondria and peroxisomes at ER contacts. It is possible that mitochondrial transport/distribution and cellular $Ca^{2+}$ dynamics may be involved in the regulation of ER–mitochondria interactions.

A previous study identified VPS13D, TSG101, and the ESCRTII component VPS36 in a genetic screen for mitophagy in *Drosophila* and further demonstrated that VPS13D acted as a key regulator of mitochondrial size and bound to tetra-ubiquitin chains through the UBA domain by in vitro pull-down assays (Anding et al., 2018). In this study, we showed that the VAB domain of VPS13D interacted with both the K63-linked and K48-linked ubiquitin chains via in vivo coimmunoprecipitation assays and confocal microscopy (Supplemental Figure S5). In addition, we demonstrated that both the UBA domain and the VAB domain interacted with p97 ATPase (Figure 3), which functioned downstream from ubiquitin signaling events (Ye et al., 2001; Jentsch and Rumpf, 2007). These results suggested that VPS13D, ubiquitin chains, and p97 might form a ternary protein complex at the ER–mitochondria contacts. In considering the contribution of VPS13D to the level of p97, we envision that deletion of one component (VPS13D) may impair the efficient assembly of the ternary protein complex, and unassembled components (p97) may

cycloheximide chase assays in H. Mean ± SD. (J) Confocal image of live U2OS cells transfected with mCherry-mito7 (red) and ER-mGFP (green) upon treatment with DMSO or p97 allosteric inhibitor NMS873 (25 µM) for 8 h. (K) Quantification of extent of MCSs in U2OS cells treated with p97 inhibitor NMS-873. For quantifications in perinuclear regions: DMSO (n = 7), 5 µM (n = 14), 10 µM (n = 10), and 25 µM (n = 9); for quantifications in peripheral regions: DMSO (n = 9), 5 µM (n = 12), 10 µM (n = 12), and 25 µM (n = 7). One-way ANOVA followed by Tukey's multiple comparisons test. Mean ± SD. (L) Confocal image of live U2OS cells transfected with mCherry-mito7 (red) and ER-mGFP (green) upon treatments with scrambled or two different p97 siRNA duplexes. (M) Immuno-blots with antibodies against p97 to demonstrate knockdown efficiency. (N) Confocal image of live U2OS cells transfected with mitoBFP (red), ER-TagRFP (green) and VPS13D siRNAs upon overexpression with GFP vector (blue) or p97-GFP (blue). (O) Quantification of extent of MCSs in U2OS cells treated with p97 siRNA, VPS13D siRNA/GFP vector, or VPS13D siRNA/p97-GFP. For quantification in perinuclear regions: scrambled (n = 13), p97 siRNA-1 (n = 21), p97 siRNA-2 (n = 23), VPS13D siRNA/GFP vector (n = 15), and VPS13D siRNA/p97-GFP (n = 21); for quantifications in peripheral regions: scrambled (n = 13), p97 siRNA-1 (n = 21), p97 siRNA-2 (n = 23), VPS13D siRNA/GFP vector (n = 15), and VPS13D siRNA/p97-GFP (n = 21). One-way ANOVA followed by Tukey's multiple comparisons test. Mean ± SD. Scale bar, 10 µm in whole-cell image and 2 µm in insets in J, L, and N.
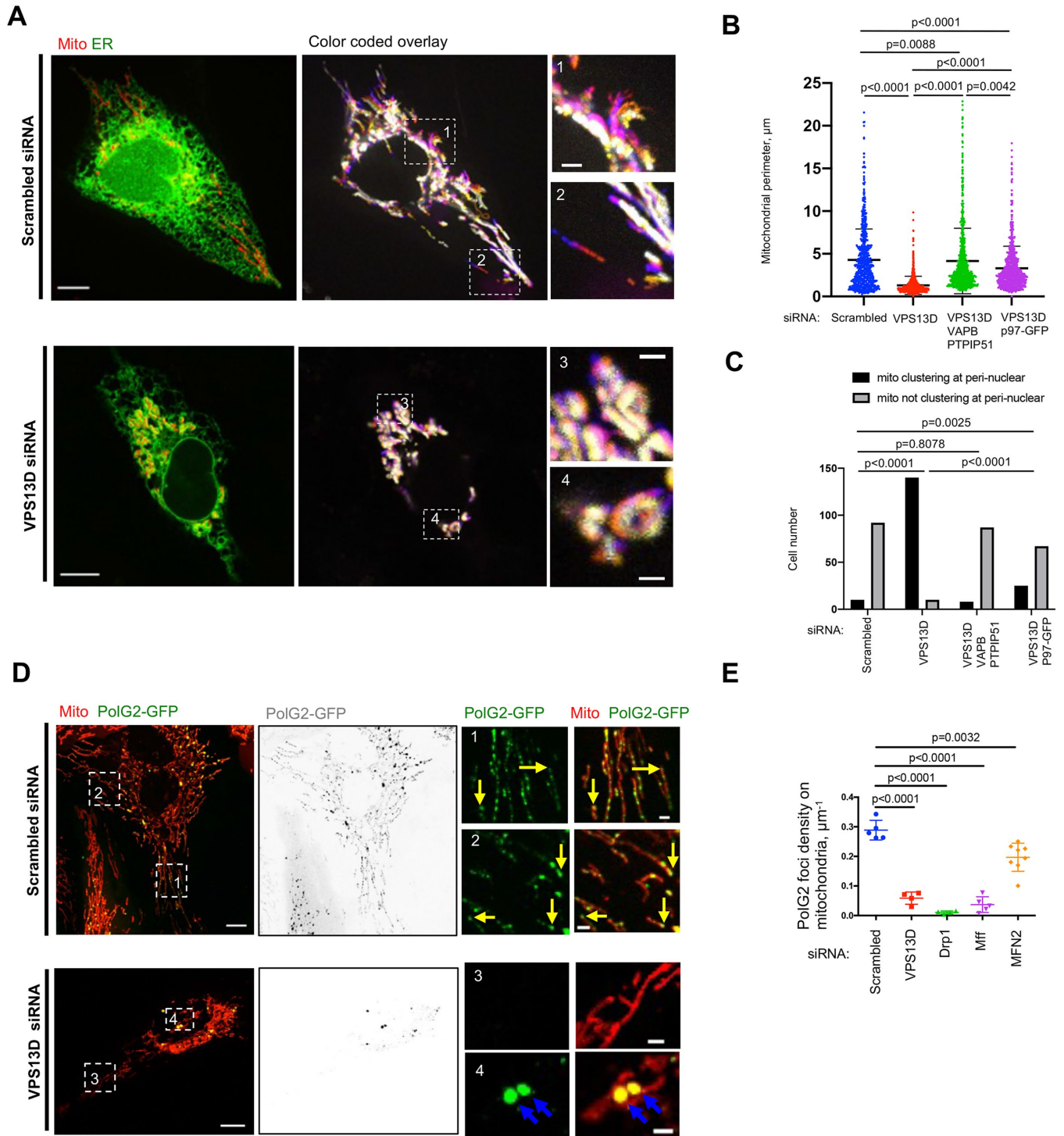
**FIGURE 4:** VPS13D suppression results in defects of mitochondrial motility, morphology, cellular distribution, and mtDNA synthesis. (A) Left: whole cell image of U2OS expressing ER (green) and mitochondrial (red) markers were treated either with scrambled or VPS13D siRNA. Right: overlays of mitochondrial dynamics time course with two insets. Colors depict time points in the sequence, with white indicating relative immobility (Supplementary Video 1). (B) Mitochondrial perimeter in scrambled siRNA (669 mitochondria from 52 cells), VPS13D siRNAs–treated U2OS cells (754 mitochondria from 53 cells), VPS13D/VAPB/PTPIP51 siRNAs–treated U2OS cells (742 mitochondria from 51 cells), and VPS13D siRNAs/p97-GFP–treated U2OS cells (746 mitochondria from 49 cells). One-way ANOVA followed by Tukey's multiple comparisons test. Mean ± SD. (C) Mitochondrial localization in scrambled siRNA (102 cells), VPS13D siRNAs–treated U2OS cells (150 cells), VPS13D/VAPB/PTPIP51 siRNAs–treated U2OS cells (95 cells), and VPS13D siRNAs/p97-GFP–treated U2OS cells (92 cells). Chi-squared and Fisher's exact tests. (D) Confocal images of live polG2-GFP stable U2OS cells expressing mCherry-mito7 (red) up treatments with scrambled (Top) or VPS13D siRNAs (Bottom). Yellow arrows indicate replicating mtDNA at mitochondrial tips in scrambled cells; blue arrows indicate

be dislocated or inactive, and may eventually be subject to degradation. Currently, we could not produce purified VAB domain proteins from either human or other organisms in sufficient quantities for biochemical analysis. Thus, we could not detect direct binding between the VAB domain and ubiquitin or p97 in vitro. Therefore, we cannot preclude the possibility that the interactions among VPS13D, p97, and ubiquitin chains are indirect.

Our results suggested that the defects in mitochondrial length or size upon VPS13D suppression (Figure 4C) could be attributed to hyperactive ER-mitochondrial interactions. This might even be true in the case of the loss of VPS13D in *Drosophila* (Anding et al., 2018). A recent study showed that reducing mitochondrial fusion by suppressing Marf (the MFN2 homolog in *Drosophila*) rescued mitochondrial size defects caused by the loss of VPS13D (Anding *et al.*, 2018). MFN2 was reported to serve as a tether at ER–mitochondria MCSs in mammals, and we speculated that Marf might also mediate ER–mitochondria interactions in *Drosophila* and that the suppression of Marf might counteract and alleviate ER–mitochondria hypertethering resulting from the loss of VPS13D in *Drosophila*. Consistently, p97 was reported to promote the degradation of MFN2 to break up ER–mitochondria MCSs before mitophagy (McLelland *et al.*, 2018). It is interesting to test whether VPS13D participates in the p97-dependent regulation of ER–mitochondria MCSs to facilitate mitophagy. Taken together, it is plausible that several mechanisms of the VPS13D-mediated regulations of ER–mitochondria MCSs exist in different scenarios and warrant further investigations.

## METHODS
Request a protocol through *Bio-protocol*.

### Plasmids and siRNA oligonucleotides
mCherry-mito7 (55102), mitoBFP (49151), p97-GFP (23971), pRK5-HA-ubiquitin-WT (17608), pRK5-HA-ubiquitin-K48 (17605), and pRK5-HA-ubiquitin-K63 (17606) were purchased from Addgene. eBFP-peroxisome was previously described (Ji *et al.*, 2017). ER-tagRFP, ER-mGFP, polG2-GFP, mStrawberry-Rab4b, mStrawberry-Rab7A, CFP-VAPB, and PTPIP51-TagBFP2 were gifts from Henry N. Higgs (Dartmouth Geisel School of Medicine). Lamp1-OFP and B4GALT1-GFP was purchased from Sinobiological. ACSL3-Halo was generated by cutting the ACSL3 ORF from pEFIRES-P-ACSL3-mCherry (Addgene 87158) and pasting it into Halo-N1 vector, which was generated by replacing GFP with Halo in mGFP-N1 (Addgene 54767). The construct for quantification of the extent of ER–mitochondria contacts was generated by inserting the mitochondrial targeting sequence fused in frame with GFP$_{1-10}$ (tom20-GFP$_{1-10}$, a gift from Tito Calì at the University of Padua) and the ER targeting sequence of Sac1 fused in frame with GFP$_{11}$ (Sac1-long linker-GFP$_{11}$, a gift from Tito Calì at the University of Padua) into two MCS sites of pCW57-MCS1-P2A-MCS2 (Addgene 89180) under control of a doxycycline-inducible promoter. The Lentivirus packaging plasmids psPAX (12260) and pMD2. G (12259) were bought from Addgene. All of the truncated mutants of VPS13D or p97 used in this study were generated by PCR using human VPS13D-myc-flag (Origene, RC205601) or p97-GFP (Addgene, 23971) as templates and cloning them into mGFP-N1 (Addgene 54767), mGFP-C1 (Addgene 54579),

or the 3*flag vector, generated by replacing GFP with a 3*flag tag in mGFP-N1 (Addgene 54767). All of constructs used in this study were generated by using a ClonExpress II One Step Cloning kit (Vazyme, C112-01). Oligonucleotides for human VPS13D siRNAs were synthesized by RiboBIO against target sequences 5'-GCAGAAGGATCCT-TAAAGA-3' (siRNA#1); 5'-GTAGCACGTTTGACATGAA-3' (siRNA#2); and 5'-CAAAGAGCCTCTACTATGA-3' (siRNA#3). Oligonucleotides for VPS13A were against sequences 5'-GGATGGGACTGGAAAT-CAA-3' (siRNA#1); 5'-GCAGCTACATTCCTCTTAA-3' (siRNA#2); and 5'-GGATAGAGCTTATGATTCA-3' (siRNA#3). Oligonucleotides for p97 were against sequences 5'-GAAUAGAGUUGUUCGGAAU-3' (siRNA#1); and 5'-GGAGGUAGAUAUUGGAAUU-3' (siRNA#2). Oligonucleotides for Drp1 were against sequences 5'-GGAACAAAG-TATCTTGCTA-3' (siRNA#1); 5'-GAAGGGTTATTCCAGTCAA-3' (siRNA#2); and 5'-GGTTGGAGATGGTGTTCAA-3' (siRNA#3). Oligonucleotides for Mff were synthesized by RiboBIO against sequences 5'-GGAGAGGATTGTTGTAGCA-3' (siRNA#1); 5'-GTACTTACGCT-GAGTGAAA-3' (siRNA#2); and 5'-GTAGCTTTCTGGCTGCTTA-3' (siRNA#3). Oligonucleotides for Mfn2 were against sequences 5'-GGCCAAACATCTTCATCCT-3' (siRNA#1); 5'-CGGTTCGACT-CATCATGGA-3' (siRNA#2); and 5'-GCGAGGAAATGCGTGAAGA-3' (siRNA#3). Oligonucleotides for VAPB were against sequences 5'-CCAACAGCGGAATCATCGA-3' (siRNA#1); 5'-ACAGCACCACG-TAGGTACT-3' (siRNA#2); and 5'-CCGATGTTGTCACCACCAA-3' (siRNA#3). Oligonucleotides for PTPIP51 were against sequences 5'-GAAGCTAGATGGTGGATGA-3' (siRNA#1); 5'-GGATGAGAGT-GCTGACTGT-3' (siRNA#2); and 5'-GCGGGACTCTGACAAAGAA-3' (siRNA#3). As a control, scrambled siRNA (Negative Control), 5'-CGUUAAUCGCGUAUAAUACGCGUAT-3' (RiboBIO) was used.

### Antibodies and reagents
Anti-GFP (1:1000, 50430-2-AP, ProteinTech), anti-Mff (17090-1-AP; ProteinTech), anti-Drp1 (#8570; CST), anti-Mfn2 (12186-1-AP; ProteinTech), anti-PTPIP51 (20641-1-AP; ProteinTech), anti-calnexin (10427-1-AP; ProteinTech), anti-COXIV (11242-1-AP; ProteinTech), anti-flag (F1804; Sigma), and anti-p97/VCP (10736-1-AP; ProteinTech) were used at 1:1000 dilutions for Western blots. Anti-VAPB (14477-1-AP; ProteinTech) was used at 1:1000 for Western blots and 1:200 for immunofluorescence. Anti-tom20 (sc-17764; Santa Cruz Biotechnology), anti-tubulin (11224-1-AP; ProteinTech), and anti-actin (60008-1-Ig, ProteinTech) were used at 1:5000 dilutions for Western blots. Anti-VPS13D (A304-691A; BETHY Laboratories) was used at 1:50 dilutions for coimmunoprecipitation and 1:100 for Western blots. The reagents NMS873 (TargetMol, T1853) and BODIPY 493/503 (Thermo Fisher, D3922) were used. Antibiotics such as G418 (10131027), puromycin (A1113803), hygromycin B (10687010), and blasticidin (A1113903) were obtained from Thermo Fisher (U.S.).

### Cell culture, transfection, and stable lines
Human osteosarcoma U2OS cells (ATCC), human embryonic kidney HEK293 cells (ATCC), African green monkey kidney fibroblast-like COS7 cell line (ATCC), and human cervical cancer HeLa cells (ATCC) were grown in DMEM (Invitrogen) supplemented with 10% fetal bovine serum (Life Technologies) and 1% penicillin/streptomycin. All

---

aggregation of replicating mtDNA in VPS13D siRNA–treated cells. (E) Quantification of the density of replicating mtDNA. The definition of density of replicating mtDNA is number of replicating mtDNA divided by the perimeter of mitochondria in the whole cell. Scrambled (*n* = 16), VPS13D siRNA (*n* = 11), Drp1 siRNA (*n* = 6), Mff siRNA (*n* = 10), and MFN2 siRNA–treated cells (*n* = 8) are analyzed. Two-tailed unpaired Student's *t* test. mean ± SD. Scale bar, 10 µm in whole-cell image and 2 µm in insets in A and D.

of the cell lines used in this study are free of mycoplasma contamination. For transfection, cells were seeded at $4 \times 10^5$ cells per well in a six-well dish ~16 h before transfection. Plasmid transfections were performed in OPTI-MEM (Invitrogen) with 2 µl Lipofectamine 2000 per well for 6 h, followed by trypsinization and replating onto glass-bottomed confocal dishes at ~$3.5 \times 10^5$ cells per well. Cells were imaged in live-cell medium (DMEM with 10%FBS and 20 mM HEPES no P/S) ~16–24 h after transfection. For all transfection experiments in this study, the following amounts of DNA were used per 3.5-cm well (individually or combined for cotransfection): 500 ng for mito-BFP, eBFP2-peroxisome, mCherry-mito7, B4GALT1-GFP, ACSL3-Halo, and Lamp1-OFP; 1000 ng for ER-tagRFP, ER-mGFP, and p97-GFP; 300 ng for mStrawberry-Rab4b and mStrawberry-Rab7A. For siRNA transfections, cells were plated on 3.5-cm dishes with density 30–40%, and 2 µl lipofectamine RNAimax (Invitrogen) and 50 ng siRNA were used per well. At 48 h after transfection, a second round of transfection was performed with 50 ng siRNAs. Cells were analyzed 24 h post–second transfection for suppression. For the generation of the stable Dox-inducible ER–mitochondria MCSs reporter U2OS cell line: day 1: 293T cells were seeded into 10-cm dish with ~$3 \times 10^6$ cells 18 h before transfection; day 2: transfections were performed with 4 µg PCW-Tom20-GFP$_{1-10}$-P2A-Sac1-long linker-GFP$_{11}$, 3 µg psPAX2, and 2 µg pMD2.G; day 3: U2OS cells were seeded into 10-cm dishes with $2 \times 10^6$ cells; day 4: the supernatant from transfected HEK293 cells was collected 48 h post–initial transfection, followed by filtering through a syringe with 0.22-µm filters, and 1 ml filtered HEK293 supernatant was added to U2OS cells; day 5: U2OS cells were grown in tetracycline-free medium containing G418 (2 µg/ml), followed by verification by imaging and Western blots. To make a polG2-GFP U2OS cell line, we transfected U2OS cells with polG2-GFP construct by lipofectamine 2000. At 24 h after transfection, cells were grown in G418 (1 µg/ml)-containing growth medium for another week, followed by fluorescence-activated cell sorting (FACS).

## Live imaging by confocal microscopy

Cells were grown on glass-bottomed confocal dishes. Confocal dishes were loaded into a laser scanning confocal microscope (LSM780, Zeiss, Germany) equipped with multiple excitation lasers (405, 458, 488, 514, 561, and 633 nm) and a spectral fluorescence GaAsP array detector. Cells were imaged with the $63 \times 1.4$-NA iPlan-Apochromat 63× oil objective using the 405-nm laser for BFP, 488-nm for GFP, and 561-nm for mStrawberry, OFP, tagRFP, or mCherry. To track the dynamics of mitochondria and ER, cells on confocal dishes were loaded into a spinning-disk confocal microscope (Olympus IX83, Japan) equipped with 100×/1.4 oil (WD 013 mm, DIC slider) objective, multiple lasers (405, 488, 561, and 640 nm) with corresponding filters, and EMCCD and scMOS cameras.

## Antibody preclearing

For endogenous VPS13D IF, anti-VPS13D antibody was first cleared according to the protocol described in (Valverde et al., 2019). Briefly, VPS13D-depleted HEK293 cells were fixed in 4% paraformaldehyde (PFA) for 15 min, rinsed with phosphate-buffered saline (PBS), quenched in 50 mM $NH_4Cl$ in PBS, washed twice with PBS, permeabilized with PBX (PBS containing 0.1% Triton X-100) for 10 min, and scraped in PBX with 1% Triton X-100. Antibodies were added to the fixed cells at the final concentration used for IF (1:100) and mixed overnight by rotation at 4°C. The mixture was then centrifuged at $17,000 \times g$ for 20 min at 4°C, and the supernatant containing cleared antibodies was used for IF.

## Quantitative RT-PCR for detecting the mRNA level of VPS13D and VPS13A

U2OS cells were transfected with either scrambled, VPS13D, or VPS13A siRNAs. At 4 d after transfection, RNA was isolated with Trizol (Thermo Fisher) according to the instructions of the manufacturer. cDNA was reverse transcribed using RverTra Ace (TRT-101, TOYOBO) according to the directions of the manufacturer. The cDNA was analyzed using quantitative PCR with qPCR Mix (QPS-201, TOYOBO) using the following primers: VPS13D-1: 5'-GTGACTGACAACAGATAC-GAGCCA-3'; 5'-CGACCAACCCATGTAACCCA-3'; VPS13D-2: 5'-TC-GATATGCAGCACCAGATAAA-3'; 5'-CTGGTGGGAGTGAAGAG-AAATAA-3'; VPS13D-3: 5'-GGATTTGCCTCAGATGGAGTTAC-3'; 5'-TCCAGGACGTAGTGATGGCT-3'; VPS13A-1: 5'-CGGTGCTATG-GCTAAG-3'; 5'-CCTCCACGAGTGATGC-3'; VPS13A-2: 5'-TGGGCT-TATGCTATACATGGCG-3'; 5'-CCAAAGACACGAGAAGTTCACC-3'; VPS13A-3: 5'-TGTGATGAATCGCCGATCTGA-3'; 5'-CCATGTATAG-CATAAGCCCACCA-3'.

## Immunofluorescence staining

Cells were fixed with 4% PFA (Sigma) in PBS for 10 min at room temperature. After being washed three times with PBS, cells were permeabilized with 0.1% Triton X-100 in PBS for 15 min on ice. Cells were then washed three times with PBS, blocked with 0.5% BSA in PBS for 1 h, incubated with primary antibodies in diluted blocking buffer overnight, and washed three times with PBS. Secondary antibodies were applied for 1 h at room temperature. After being washed three times with PBS, samples were mounted on Vectashield (H-1000; Vector Laboratories).

## Image analysis

All image analysis and processing were performed using ImageJ (National Institutes of Health). Colocalization-based analysis of ER–mitochondria contacts was performed by a colocalization plugin (imageJ, NIH) with the following settings: ratio (0–100%): 50; threshold channel 1 (0–255): 50; threshold channel 2 (0–255): 50; display value (0–255): 255. ER–mitochondria intersection sites were automatically identified by the colocalization plugin, with white pixels representing potential ER–mitochondria contact sites. For mitochondrial perimeter measurement, an imageJ macro named the mitochondrial morphology macro (Dagda et al., 2008) was used to measure the perimeter of mitochondria in regions of interest (ROIs) where mitochondria are well resolved. For the measurement of polG2-GFP–labeled replicating mitochondrial DNA density in mitochondria, two steps were performed. Step1: measure the number of polG2-GFP puncta by cell counter (imageJ plugin, NIH) in ROIs; step2: measure the mitochondrial perimeters of corresponding ROIs. The density of replicating mitochondrial DNA was calculated as the number of polG2-GFP puncta divided by the perimeter of mitochondria in a ROI.

## Differential centrifugation

Differential centrifugation was a modified version of the protocol previously described (Ji et al., 2017). Cells were harvested from $2 \times 10$ cm$^2$ dishes at 90% confluency. The following steps were conducted at 4°C or on ice. Cells were washed with precold PBS twice and homogenized in isolation buffer (225 mM mannitol, 75 mM sucrose, 0.1 mM EGTA, 30 mM Tris-HCl pH7.4) by Dounce (Wheaton Dura-Grind). The homogenate was centrifuged twice for 10 min at $600 \times g$ to remove nuclei and debris. The resulting supernatant was centrifuged three times for 15 min at $13,000 \times g$ to obtain crude mitochondria. Western blotting was performed using rabbit anti-VAPB (1:1000, 14477-1-AP, ProteinTech), rabbit anti-PTPIP51

(1:1000, 20641-1-AP, ProteinTech), rabbit anti-p97 (1:1000, 10736-1-AP, ProteinTech), rabbit anti-calnexin (1:500, 10427-2-AP, Protein-Tech), anti-Lamp1 (1:1000; sc-20011;Santa Cruz Biotechnology), anti-Rab7A (1:1000; A12784; ABclonal), anti-HSP60 (1:1000; 15282-1-AP; ProteinTech), and rabbit anti-COXIV (1000, 11242-1-AP, Pro-teinTech) antibodies.

## Electron microscopy
Scrambled or VPS13D siRNA–treated U2OS cells were fixed with 2.5% glutaraldehyde in 0.1 M phosphate buffer, pH 7.4 for 2 h at room temperature. After being washed three times with 0.1 M phosphate buffer, cells were scraped and collected with 0.1 M phosphate buffer followed by centrifugation at 3000 rpm. The pellet was resuspended in PBS (0.1 M) and centrifuged at 3000 rpm for 10 min. This step was repeated three times. The samples were postfixed with precold 1% OsO4 in 0.1 M phosphate buffer for 2–3 h at 4°C, followed by rinsing three times with PBS for 20 min. The samples were dehydrated in graded ethanol (50%, 70%, 85%, 90%, 95%, $2 \times 100\%$) for 15 min for each condition. The penetrations were performed in the order acetone-epoxy (2:1); acetone-epoxy (1:1); epoxy. Each round of penetration was performed at 37°C for 12 h. The samples were embedded in epoxy resin using standard protocols (Kumar *et al.*, 2014). Sections parallel to the cellular monolayer were obtained using a Leica EM UC7 with a thickness of 60–100 nm and examined under a Tecnai G2 20 TWIN (FEI) with accelerating voltage 200 kV. Mitochondria and ER were identified based on their respective morphologies and were traced by hand. The extension length of ER–mitochondria contact regions was measured using the "measure" tool in ImageJ (NIH)s. Mitochondria with ER within 30 nm at any point on the mitochondrial circumference were identified as contact sites.

## Green fluorescent protein–trap assay
GFP-trap assays performed according to the manufacturer's protocol (GFP-trap agarose beads, ChromoTek) were used for detection of protein–protein interactions. The 5% input was used in GFP traps unless otherwise indicated.

## Statistical analysis
All statistical analyses and *p*-value determinations were performed in GraphPad Prism6. To determine *p*-values, ordinary one-way ANOVA with Turkey's multiple comparisons test was performed among multiple groups and a two-tailed unpaired Student's *t* test was performed between two groups. Chi-squared analysis followed by Fisher's exact tests was performed in Figure 4C and Supplemental Figure S3C.

## Data availability
All the data and relevant materials, including constructs and primers, that support the findings of this study are available from the corresponding author upon reasonable request.

## REFERENCES
Abrisch RG, Gumbin SC, Wisniewski BT, Lackner LL, Voeltz GK (2020). Fission and fusion machineries converge at ER contact sites to regulate mitochondrial morphology. J Cell Biol 219, e201911122.

Anding AL, Wang C, Chang TK, Sliter DA, Powers CM, Hofmann K, Youle RJ, Baehrecke EH (2018). Vps13D encodes a ubiquitin-binding protein that is required for the regulation of mitochondrial size and clearance. Curr Biol 28, 287–295.e286.

Area-Gomez E, Del Carmen Lara Castillo M, Tambini MD, Guardia-Laguarta C, de Groof AJ, Madra M, Ikenouchi J, Umeda M, Bird TD, Sturley SL, Schon EA. (2012). Upregulated function of mitochondria-associated ER membranes in Alzheimer disease. EMBO J 31, 4106–4123.

Baldwin HA, Wang C, Kanfer G, Shah HV, Velayos-Baeza A, Dulovic-Mahlow M, Bruggemann N, Anding A, Baehrecke EH, Maric D, *et al.* (2021). VPS13D promotes peroxisome biogenesis. J Cell Biol 220, e202001188.

Baron Y, Pedrioli PG, Tyagi K, Johnson C, Wood NT, Fountaine D, Wightman M, Alexandru G (2014). VAPB/ALS8 interacts with FFAT-like proteins including the p97 cofactor FAF1 and the ASNA1 ATPase. BMC Biol 12, 39.

Bekris LM, Yu CE, Bird TD, Tsuang DW (2010). Genetics of Alzheimer disease. J Geriatr Psychiatry Neurol 23, 213–227.

Cali T, Ottolini D, Vicario M, Catoni C, Vallese F, Cieri D, Barazzuol L, Brini M (2019). splitGFP technology reveals dose-dependent ER–mitochondria interface modulation by alpha-synuclein A53T and A30P mutants. Cells 8, e8091072.

Chen HJ, Anagnostou G, Chai A, Withers J, Morris A, Adhikaree J, Pennetta G, de Belleroche JS (2010). Characterisation of the properties of a novel mutation in VAPB in familial ALS. J Biol Chem 285, 795–809.

Cieri D, Vicario M, Giacomello M, Vallese F, Filadi R, Wagner T, Pozzan T, Pizzo P, Scorrano L, Brini M, Cali T (2018). SPLICS: A split green fluorescent protein-based contact site sensor for narrow and wide heterotypic organelle juxtaposition. Cell Death Differ 25, 1131–1145.

Csordas G, Renken C, Varnai P, Walter L, Weaver D, Buttle KF, Balla T, Mannella CA, Hajnoczky G (2006). Structural and functional features and significance of the physical linkage between ER and mitochondria. J Cell Biol 174, 915–921.

Csordas G, Varnai P, Golenar T, Roy S, Purkins G, Schneider TG, Balla T, Hajnoczky G (2010). Imaging interorganelle contacts and local calcium dynamics at the ER–mitochondrial interface. Mol Cell 39, 121–132.

Dagda RK, Zhu J, Kulich SM, Chu CT (2008). Mitochondrially localized ERK2 regulates mitophagy and autophagic cell stress: implications for Parkinson's disease. Autophagy 4, 770–782.

de Brito OM, Scorrano L (2008). Mitofusin 2 tethers endoplasmic reticulum to mitochondria. Nature 456, 605–610.

De Vos KJ, Morotz GM, Stoica R, Tudor EL, Lau KF, Ackerley S, Warley A, Shaw CE, Miller CC (2012). VAPB interacts with the mitochondrial protein PTPIP51 to regulate calcium homeostasis. Hum Mol Genet 21, 1299–1311.

Filadi R, Greotti E, Turacchio G, Luini A, Pozzan T, Pizzo P (2016). Presenilin 2 modulates endoplasmic reticulum–mitochondria coupling by tuning the antagonistic effect of mitofusin 2. Cell Rep 15, 2226–2238.

Freyre CAC, Rauher PC, Ejsing CS, Klemm RW. (2019). MIGA2 links mitochondria, the ER, and lipid droplets and promotes de novo lipogenesis in adipocytes. Mol Cell 76, 811–825.e814.

Friedman JR, Lackner LL, West M, DiBenedetto JR, Nunnari J, Voeltz GK (2011). ER tubules mark sites of mitochondrial division. Science 334, 358–362.

Gauthier J, Meijer IA, Lessel D, Mencacci NE, Krainc D, Hempel M, Tsiakas K, Prokisch H, Rossignol E, Helm MH, *et al.* (2018). Recessive mutations in >VPS13D cause childhood onset movement disorders. Annals of neurology 83, 1089–1095.

Guardia-Laguarta C, Area-Gomez E, Rub C, Liu Y, Magrane J, Becker D, Voos W, Schon EA, Przedborski S (2014). alpha-Synuclein is localized to mitochondria-associated ER membranes. J Neurosci 34, 249–259.

Guillen-Samander A, Leonzino M, Hanna MG, Tang N, Shen H, De Camilli P (2021). VPS13D bridges the ER to mitochondria and peroxisomes via Miro. J Cell Biol 220, e202010004.

Hamasaki M, Furuta N, Matsuda A, Nezu A, Yamamoto A, Fujita N, Oomori H, Noda T, Haraguchi T, Hiraoka Y, *et al.* (2013). Autophagosomes form at ER–mitochondria contact sites. Nature 495, 389–393.

Hirabayashi Y, Kwon SK, Paek H, Pernice WM, Paul MA, Lee J, Erfani P, Raczkowski A, Petrey DS, Pon LA, Polleux F (2017). ER–mitochondria tethering by PDZD8 regulates Ca(2+) dynamics in mammalian neurons. Science 358, 623–630.

Iwasawa R, Mahul-Mellier AL, Datler C, Pazarentzos E, Grimm S (2011). Fis1 and Bap31 bridge the mitochondria–ER interface to establish a platform for apoptosis induction. EMBO J 30, 556–568.

Jentsch S, Rumpf S (2007). Cdc48 (p97): A "molecular gearbox" in the ubiquitin pathway? Trends Biochem Sci 32, 6–11.

Ji WK, Chakrabarti R, Fan X, Schoenfeld L, Strack S, Higgs HN (2017). Receptor-mediated Drp1 oligomerization on endoplasmic reticulum. J Cell Biol 216, 4123–4139.

Kornmann B, Currie E, Collins SR, Schuldiner M, Nunnari J, Weissman JS, Walter P (2009). An ER–mitochondria tethering complex revealed by a synthetic biology screen. Science 325, 477–481.

Kumar N, Leonzino M, Hancock-Cerutti W, Horenkamp FA, Li P, Lees JA, Wheeler H, Reinisch KM, De Camilli P (2018). VPS13A and VPS13C are lipid transport proteins differentially localized at ER contact sites. J Cell Biol 217, 3625–3639.

Kumar S, Ciraolo G, Hinge A, Filippi MD (2014). An efficient and reproducible process for transmission electron microscopy (TEM) of rare cell populations. J Immunol Methods 404, 87–90.

Lewis SC, Uchiyama LF, Nunnari J (2016). ER–mitochondria contacts couple mtDNA synthesis with mitochondrial division in human cells. Science 353, aaf5549.

Liu Y, Ma X, Fujioka H, Liu J, Chen S, Zhu X (2019). DJ-1 regulates the integrity and function of ER–mitochondria association through interaction with IP3R3-Grp75-VDAC1. Proc Natl Acad Sci USA 116, 25322–25328.

McLelland GL, Goiran T, Yi W, Dorval G, Chen CX, Lauinger ND, Krahn AI, Valimehr S, Rakovic A, Rouiller I, et al. (2018). Mfn2 ubiquitination by PINK1/Parkin gates the p97-dependent release of ER from mitochondria to drive mitophagy. Elife 7, e32866.

Murley A, Lackner LL, Osman C, West M, Voeltz GK, Walter P, Nunnari J (2013). ER-associated mitochondrial division links the distribution of mitochondria and mitochondrial DNA in yeast. Elife 2, e00422.

Paillusson S, Gomez-Suaga P, Stoica R, Little D, Gissen P, Devine MJ, Noble W, Hanger DP, Miller CCJ. (2017). alpha-Synuclein binds to the ER–mitochondria tethering protein VAPB to disrupt Ca(2+) homeostasis and mitochondrial ATP production. Acta Neuropathol 134, 129–149.

Papiani G, Ruggiano A, Fossati M, Raimondi A, Bertoni G, Francolini M, Benfante R, Navone F, Borgese N (2012). Restructured endoplasmic reticulum generated by mutant amyotrophic lateral sclerosis-linked VAPB is cleared by the proteasome. J Cell Sci 125, 3601–3611.

Radu Stoica KJDV, Paillusson S, Mueller S, Sancho RM, Lau K-F, Vizcay-Barrena G, Lin W-L, Xu Y-F, Lewis J, Dickson DW, et al. (2014). ER–mitochondria associations are regulated by the VAPB–PTPIP51

interaction and are disrupted by ALS/FTD-associated TDP-43. Nat Commun 5, e4996.

Seong E, Insolera R, Dulovic M, Kamsteeg EJ, Trinh J, Bruggemann N, Sandford E, Li S, Ozel AB, Li JZ, et al. (2018). Mutations in VPS13D lead to a new recessive ataxia with spasticity and mitochondrial defects. Ann Neurol 83, 1075–1088.

Stoica R, De Vos KJ, Paillusson S, Mueller S, Sancho RM, Lau KF, Vizcay-Barrena G, Lin WL, Xu YF, Lewis J, et al. (2014). ER–mitochondria associations are regulated by the VAPB–PTPIP51 interaction and are disrupted by ALS/FTD-associated TDP-43. Nat Commun 5, 3996.

Stolz A, Hilt W, Buchberger A, Wolf DH (2011). Cdc48: A power machine in protein degradation. Trends Biochem Sci 36, 515–523.

Szabadkai G, Bianchi K, Varnai P, De Stefani D, Wieckowski MR, Cavagna D, Nagy AI, Balla T, Rizzuto R (2006). Chaperone-mediated coupling of endoplasmic reticulum and mitochondrial Ca2+ channels. J Cell Biol 175, 901–911.

Valverde DP, Yu S, Boggavarapu V, Kumar N, Lees JA, Walz T, Reinisch KM, Melia TJ. (2019). ATG2 transports lipids to promote autophagosome biogenesis. J Cell Biol 218, 1787–1798.

Vance JE (1990). Phospholipid synthesis in a membrane fraction associated with mitochondria. J Biol Chem 265, 7248–7256.

Wang J, Fang N, Xiong J, Du Y, Cao Y, Ji WK. (2021). An ESCRT-dependent step in fatty acid transfer from lipid droplets to mitochondria through VPS13D–TSG101 interactions. Nat Commun 12, 1252.

Xu L, Wang X, Zhou J, Qiu Y, Shang W, Liu JP, Wang L, Tong C (2020). Miga-mediated endoplasmic reticulum–mitochondria contact sites regulate neuronal homeostasis. Elife 9, e56584.

Ye Y, Meyer HH, Rapoport TA (2001). The AAA ATPase Cdc48/p97 and its partners transport proteins from the ER into the cytosol. Nature 414, 652–656.

Young MJ, Humble MM, DeBalsi KL, Sun KY, Copeland WC (2015). POLG2 disease variants: Analyses reveal a dominant negative heterodimer, altered mitochondrial localization and impaired respiratory capacity. Hum Mol Genet 24, 5184–5197.

Zampese E, Fasolato C, Kipanyula MJ, Bortolozzi M, Pozzan T, Pizzo P (2011). Presenilin 2 modulates endoplasmic reticulum (ER)–mitochondria interactions and Ca2+ cross-talk. Proc Natl Acad Sci USA 108, 2777–2782.

Zhang YW, Thompson R, Zhang H, Xu H (2011). APP processing in Alzheimer's disease. Mol Brain 4, 3.